ARTICLE

Received 00th January 20xx,
Accepted 00th January 20xx

DOI: 10.1039/x0xx00000x

Atomistic modeling of metal-ligand chirality transfer and chiroptical properties of lead and tin hybrid perovskites

Mariagrazia Fortino,[a] Alessandro Mattoni [b*] and Adriana Pietropaolo [a*]

Hybrid organic–inorganic perovskites have emerged as excellent material for solar cell implementations. Indeed, their extreme tunability and facile synthesis open the door to many new applications. Chiral hybrid perovskites are attracting great interest as promising chiroptoelectronics systems with perspectives for optoelectronic, spintronics, among others. To date the mechanism through which the chiral bias is generated from the chiral organic ligand to the inorganic lattice is unclear. Herein we present a bespoke simulation workflow based on DFT and TD-DFT for the study of the chiroptical response of lead- and tin-based 2D chiral perovskites, namely the 2D R- and S-$(MBA^+)_2PbI_4$ and R- and S-$(MBA^+)_2SnI_4$. The most impacting factors influencing their CD signals were explored through ab-initio molecular dynamics simulations and analysis of the density of electronic states (DOSs) showing that the relevant chiroptical features are associated to a chirality transfer event driven by a metal-ligand overlap of electronic levels. This effect is more evident for the tin-based chiral perovskites showing higher chirality with excitonic coupling, starting from the chiral ligands propagating within the inorganic layer. The difference between tin and lead is due to the higher mixing of metal-ligand electronic states of the tin chiral perovskite, inducing chiroptical signals with wavelengths of 350-500 nm. These signals are red-shifted within the range of 500-600 nm for the lead chiral perovskite. The high electronic coupling between the chiral ligands and the tin octahedra can be ascribed from a radically different assembling of the chiral ligands encapsulated in the tin perovskite, resulting in a highly distorted coordination forming CH-π interactions with distance values of 3.2 Å, not formed in the lead-based system.

Introduction

In the recent years, hybrid organic–inorganic perovskites have spearheaded the field of material science for optoelectronics, owing to the highly tunable band gap, strong quantum confinement effect, as well as high optical absorption coefficients.[1-4] In addition to the excellent performances in the photovoltaics field, the large absorption coefficients, good charge transport properties and resilience to defects of these materials have attracted considerable attention also for their use in developing high-performance optoelectronic devices such as light-emitting diodes,[5-10], photonic lasers,[11-13] photodetectors[14-19] and solar cells.[20-22] In particular, low-dimensional hybrid perovskites (LDHPs) have shown to possess unique electrical and optical properties easily tuned by controlling their structure and size compared to their 3D counterpart.[23-27]

Very recently, new roots of applications for LDHPs particularly the 2D frameworks, have emerged when embedding chiral organic ligands in the inorganic polyhedra.[28-34] A chiral bias has been postulated to originate from the chiral ligand, thereby propagating towards the inorganic scaffold, inducing a chiroptical response from the inorganic metal-halide sublattice.[35,36] Different explanation have been proposed: i) a geometrical distortion of the inorganic lattice with a consecutive chirality transfer event;[37] ii) the coupling of the static dipole of the chiral ligand to the transition dipole moment of the perovskite cluster;[38] iii) restricted molecular rotations of the organic ligand inducing distortions,[39] enhancing the asymmetry with halogen substitutions at the aliphatic carbon;[40] iv) generation of helical chirality into the entire perovskite frameworks;[41] v) micro-strain affecting the electronic interactions between the inorganic building blocks and the chiral organic spacer. [42]

The most studied chiral hybrid perovskite is undoubtedly the one embedding methylbenzyl ammonium (MBA^+) as chiral organic ligand within the $[PbI_6]^{2-}$ inorganic layer, displacing important opposite circular dichroism (CD) [35,41,43] and circularly polarized luminescence (CPL) signals,[43] for the corresponding R-

[a] Dipartimento di Scienze della Salute, Università di Catanzaro, Catanzaro (CZ), Italy.
[b] Istituto Officina dei Materiali (CNR-IOM), Unità di Cagliari, Cittadella Universitaria, Monserrato (CA), Italy.

Email:apietropaolo@unicz.it; mattoni@iom.cnr.it
Electronic Supplementary Information (ESI) available:
See DOI: 10.1039/x0xx00000x

and S- enantiomers. Noteworthy, recent CD measurements on lead-free non-toxic alternatives have shown a chiroptical activity in the 300-500 nm wavelength range with significative opposite signals for the R- and S-$(MBA^+)_2SnI_4$ enantiomers.[44] Despite the importance of these chiral hybrid nanomaterials, the elucidation of their fundamental chiroptical properties inducing the chiral bias mechanisms is today unclear.[39,45-47] In this scenario, considering the importance of chiral information and asymmetry transmission across the inorganic structural perovskite motifs, atomistic modeling can contribute in the research for innovative technologies based on chiral hybrid perovskites. Ab-initio methods based on density functional theory (DFT) and its time-dependent extension (TD-DFT) may lead to an accurate analysis and prediction of structural, electronic and physical-chemical properties of chiral LDHPs.

Herein we present a simulation workflow based on ab-initio molecular dynamics, analysis of electronic density of states (DOSs) and TD-DFT simulations in order to disclose the main features impacting the electronic transitions. DOSs calculations have revealed subtle differences between the lead- and tin-based chiral LDHPs. Indeed, for lead- and in more extent for tin-based chiral LDHPs a chirality transfer event originated from metal-ligand interactions of electronic states affecting the chiroptical features. The electronic circular dichroism (ECD) spectra were predicted at the TD-DFT level for representative molecular clusters of the 2D R- and S-$(MBA^+)_2PbI_4$ and R- and S-$(MBA^+)_2SnI_4$. A good agreement with the available experimental data[43,44] highlights that the inclusion of two octahedral inorganic layers and four chiral ligands is already a representative model for the description of the electronic and CD signals.

Results and Discussion

The density of states calculated at the PBE[48] level of theory including spin orbit coupling[49] (SOC) using periodic boundary conditions (PBC) and projected on the Pb and Sn atoms of the inorganic layer and on the C atoms belonging to the MBA^+ ligands of the lead- and tin- based chiral LDHPs are reported in Figure 1. Specifically, in panel 1a of Figure 1 we report the electronic density of states projected (PDOSs) on the metal (left) and aromatic carbon atoms (right) computed for the whole lead- and tin- based chiral LDHPs.

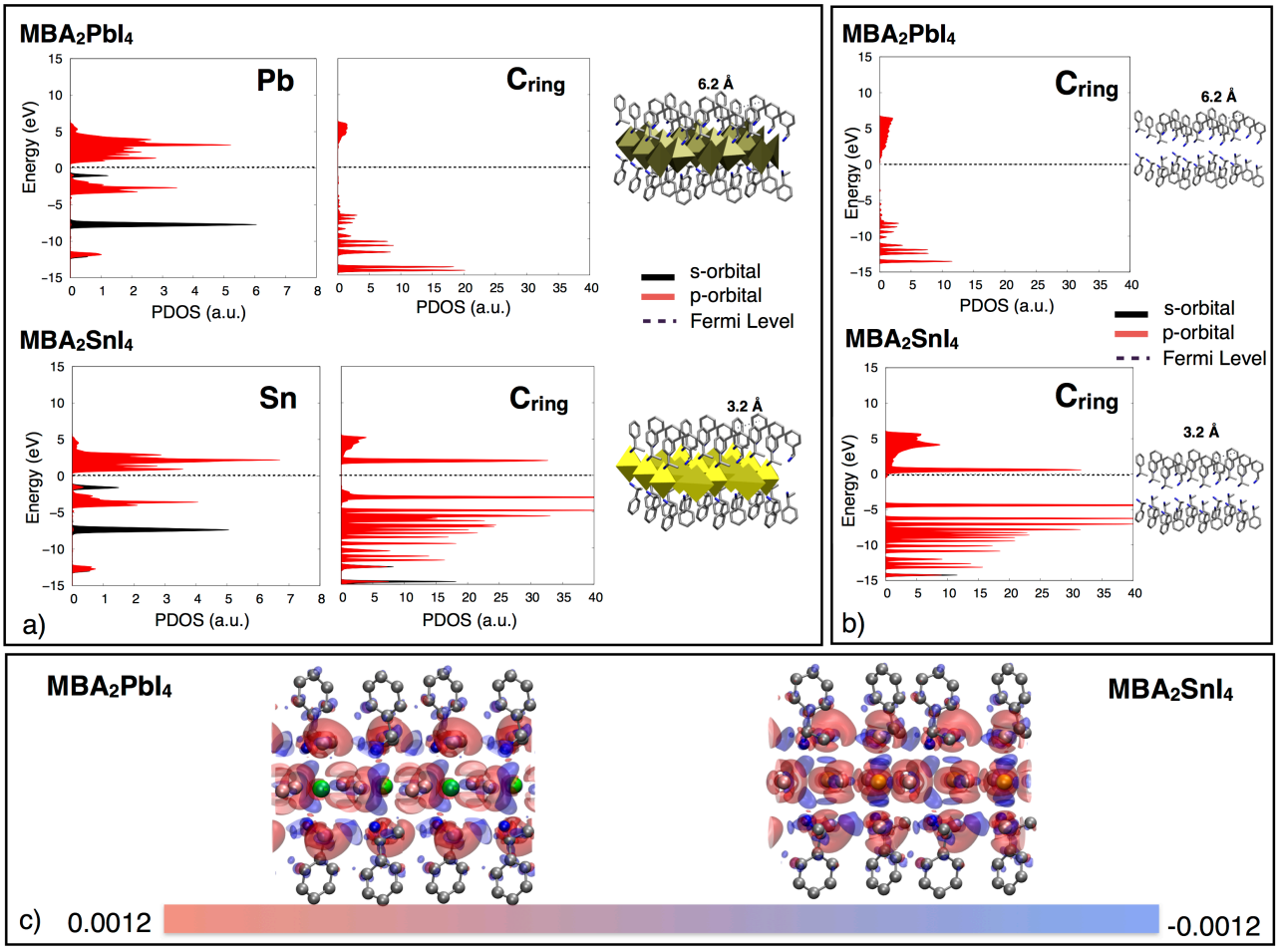

Figure 1. a) PDOS computed at PBE level of theory within SOC with periodic boundary conditions for the whole lead- and tin- based chiral LDHPs, projected on Pb, Sn and C atoms belonging to MBA^+ ligands; b) PDOS computed at PBE level of theory within SOC in PBC projected on C atoms belonging to MBA^+ ligands, excluding the inorganic layers. The molecular structures shown are relative to the S enantiomers of the MBA^+. All the reported DOS have been aligned respect to the computed Fermi level. c) Electron density difference $\Delta\boldsymbol{\rho}$ computed for S-$(MBA^+)_2PbI_4$ and S-$(MBA^+)_2SnI_4$ perovskites; this is obtained by subtracting the electron densities of the inorganic layers and the organic ligands to the total density ($\Delta\boldsymbol{\rho} = \boldsymbol{\rho}_{TOT} - \boldsymbol{\rho}_{octahedra} - \boldsymbol{\rho}_{MBA^+}$). Blue regions correspond to negative isovalues, while red region to positive isovalues.

The PDOSs on aromatic carbon atoms are computed for the sole chiral ligands by excluding the inorganic layers (Figure 1b). The calculated PDOSs show a sizeable metal-ligand interaction of electronic states, in both lead- and tin-based chiral LDHPs associated to a chirality transfer occurring in the hybrid systems. More specifically, the density of states projected on the C atoms of the ligand rings and calculated for the whole perovskite systems give rise to bands shifted in the higher region of the conduction level and with less intensity compared to the same calculations repeated on the systems without the inorganic layer. This result is much more evident for the tin-based chiral LDHP system. In particular the peaks near the Fermi level of the sole ligands appear shifted with higher energy in the DOS of hybrid systems, with a sharp peak approaching 1.5 eV for the tin-based perovskite (Figure 1 a). Noteworthy, a partial energy transfer from the inorganic lattice to the organic chromophore was recently proposed in tetrazine-based achiral lead perovskite.[50] To further clarify the electronic coupling between the inorganic and the organic moieties mainly observed for the tin-based perovskites, the electron density differences have been computed and shown in Figure 1c. The electron density differences were calculated as the difference of the electron densities of the whole chiral perovskite systems and the electron densities of the inorganic layer and the organic ligand (further details are reported in the Supplementary Information), disclosing a redistribution of the electronic density as a result of the organic/inorganic interaction in both lead and tin chiral perovskites. It is observed a charge shift from the aromatic ring towards the methylammonium groups and an expansion of charge on the halides indicating the enhancement of salt-bridge ion pair interactions. To the best of our knowledge no quantum chemistry package taking account periodic boundary conditions is currently available for the calculations of rotational strengths, that can result highly demanding.

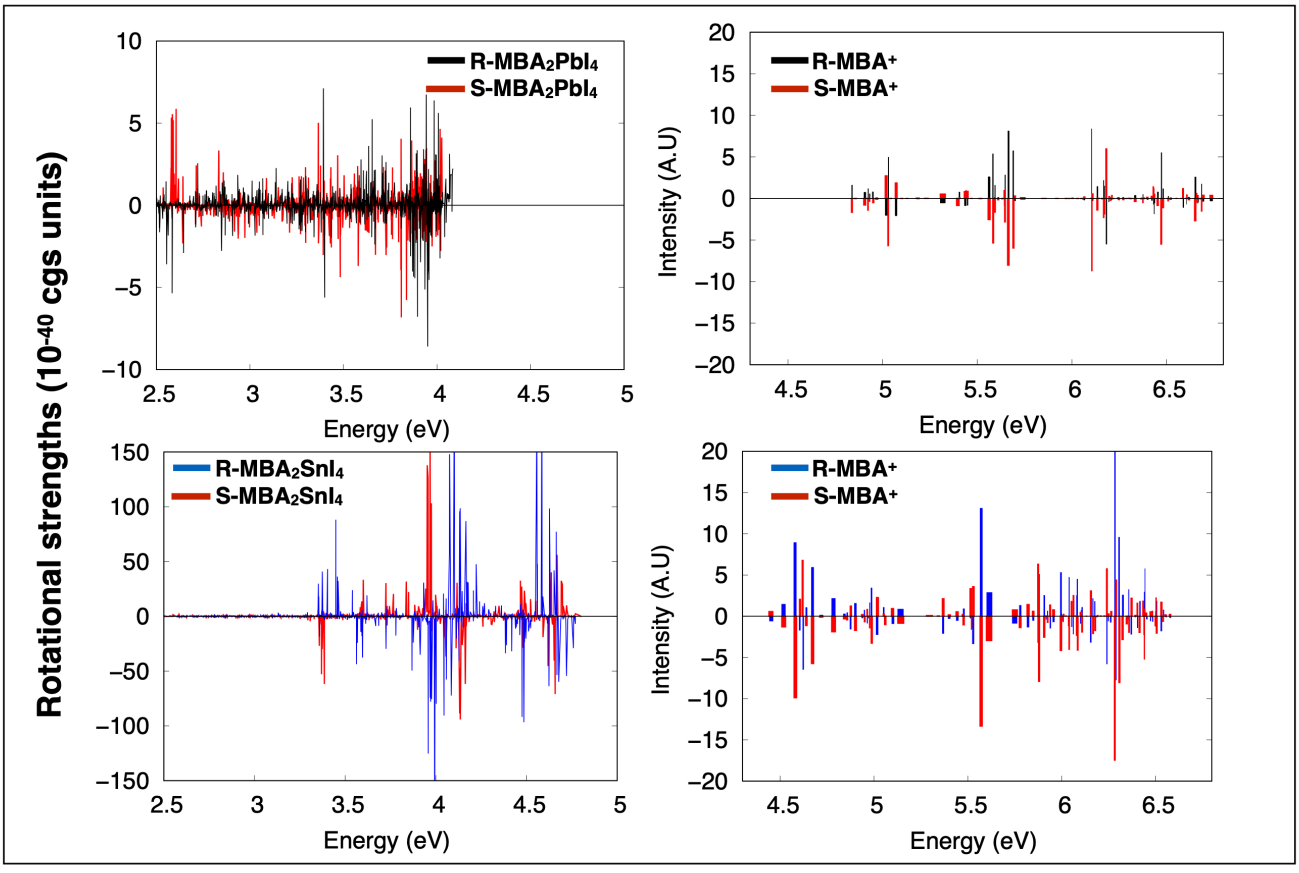

Figure 2. a) Excitonic lines calculated for the whole lead- and tin- based chiral LDHPs and for the chiral organic ligands (cluster model). The rotational strengths calculated for the tin perovskite are ten times higher than those calculated for the lead analogue.

Although layered perovskites need to account for periodic simulations when studying semiconductor properties[51] directly linked to ionic mobility[52] or transport charge,[53] chiroptical properties may have a more local nature subtly depending on the helix pitch within chemical coordinates and the generated coupling between magnetic and electric transition dipole moments.[54] Therefore, to investigate the chiroptical features for 2D R- and S-$(MBA^+)_2PbI_4$ and R- and S-$(MBA^+)_2SnI_4$, we combined DFT and TD-DFT calculations on representative molecular clusters, that account for the typical helix pitch of the perovskite coordinates. The chosen models consist of two inorganic $[MI_6]^{4-}$ (with $M=Pb^{2+}$ or Sn^{2+}) octahedral layers and four chiral MBA^+ chains into the R and S enantiomeric models; such models maintain the 2:1 stoichiometric ligand-perovskite ratio experimentally reported and represents a compromise between simulation cost and material representativeness. In principle, in order to approximate the properties of infinite periodic layers it is necessary to take into account large clusters; however, as far as concern transitions relevant for CD as it will be shown below the use of small clusters is already meaningful. The DOSs computed in periodic conditions and the DOSs computed for the molecular clusters of lead- and tin- based perovskites are reported in Figure S1 of the Supplementary Information. The DOSs of the optimized clusters exhibit larger gaps with respect to the PBC layers due to the expected quantum confinement effect; however the gap of the cluster is still free of intra-gap levels and the bands are not dramatically affected with respect to the pbc layers. It is worth to remark the importance of SOC contributions. The latter tend to close the gap and coupled with beyond-DFT treatment including GW, DFT+1/2 or VPSIC (that opens the gap) are necessary especially for tin hybrids in which the two effects do not compensate as is instead the case of lead (https://pubs.rsc.org/en/content/articlehtml/2021/ta/d1ta01573g ; https://pubs.acs.org/doi/10.1021/acs.jpcc.1c09594). In acluster representation of the chiral material the gap is likely overestimated because of the quantum confinement effects and the solely inclusion of SOC already tends to correct the results. Furthermore, the excitonic transitions are much higher than the energy gap and the approximations of the cluster model are less dramatic. In particular, the terminations of the cluster do not induce deep localized states but affects the band extrema, consistently with the well-known defect tolerance of metal halides.

Since thermal effects are expected to be relevant for chiral perovskites and their chiroptical properties, we perform ab-initio molecular dynamics simulations at PBE level of theory, on such lead- and tin-based chiral perovskite models. Ab initio molecular dynamics describes accurately the nuclei trajectories and makes it possible to include in our calculations the effect of distortions (though on a limited timescale). From the computed ab-initio trajectories, a representative set of configurations have been extracted and used to calculate at the HSE06/LANL2DZ level of theory, the transition energies, the oscillator and the rotatory strengths from the ground to the excited states, for the prediction of the absorption UV-vis and ECD spectra. Those together with the experimental spectra extracted from the study conducted by Ma et al.[43] are reported in Figure 3.

The excitation energies of the hybrid system related to the electronic coupling and calculated for a cluster model including two octahedra and four chiral ligands fall in the region between 2.5 eV and 5.0 eV, whereas those of the chiral ligands fall within 4.5 eV and 6.5 eV. The values of the rotational strengths calculated for the chiral ligands increase within inorganic octahedra, resulting ten times higher in the presence of tin octahedra (Figure 2a). A further analysis of the tin- and the lead-based chiral LDHP molecular structures suggests an explanation of the observed differences in terms of metal-ligand interaction. The tin-based chiral LDHP system shows radical morphological differences if compared with the lead analogue. The inorganic layers of the chiral tin perovskite show larger level of octahedral bond distortion.[44] Furthermore the organic ligands display significant differences of molecule assembling if compared with the lead-based system. Such evidence can be ascribed to CH-π interactions of the chiral ligands observed in the tin-based perovskite with distance values of 3.2 Å. This spacing of the ligands is present in the tin LDPHs crystallized structures[44] together with the structural models herein reported and it is presumably related to the highly distorted geometry of the coordination octahedra of the layered Sn-I perovskite. For this reason, these contacts are not revealed in the lead-based system, showing distance values approaching 6.2 Å.

The UV-vis and ECD spectra simulated on small molecular clusters already reproduce the experimental spectra, indicating that to simulate the circular dichorism spectra the minimum requirement is a unitary cell model preserving the helix pitch, in this case the 2_1 axis with at least two octahedral inorganic layers and four chiral ligands.

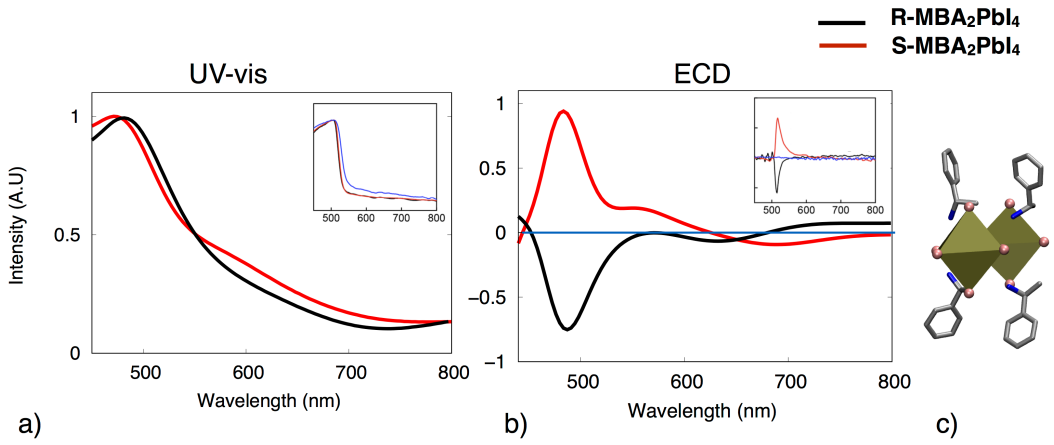

Figure 3. a) UV-vis and b) ECD spectra computed by using a representative set of configurations extracted from the ab-initio trajectories in order to adequately describe the ground states of S- and R- $(MBA^+)_2PbI_4$ coordinates; c) a sketch of the investigated models. In the inset, the experimentally available UV-vis and ECD spectra are also reported.[43] Reprinted with permissions from Reference[43] Copyright 2022 ACS Publications.

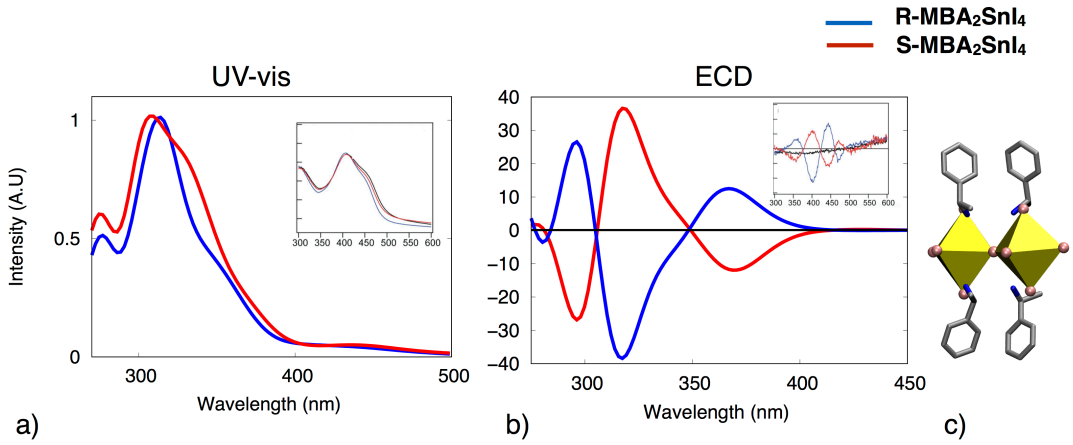

Figure 4. a) UV-vis and b) ECD spectra computed by using a representative set of configurations extracted from the ab-initio trajectories in order to adequately describe the ground states of S- and R- $(MBA^+)_2SnI_4$ coordinates; c) a sketch of the investigated models. In the inset, the experimentally available UV-vis and ECD spectra are also reported. [44] Reprinted with permissions from Reference[44] Copyright 2022 ACS Publications.

The computed UV-vis spectra exhibit an absorption band located at 490 nm showing a good agreement with the experimental ones having a band at 510 nm.[43] The agreement with the experimental spectra is also observed with the calculated ECD spectra, predicted to have a prominent positive signal at 490 nm for the S-$(MBA^+)_2PbI_4$ enantiomer and a negative one in the same position for the R-$(MBA^+)_2PbI_4$ enantiomer. The calculated absorption UV-vis and ECD spectra together with the experimental spectra, extracted from the study conducted by Lu et al.[44] of the tin-based chiral perovskite are reported in Figure 4. Similarly for the lead case calculations those were obtained from a collection of configurations extracted from the ab-initio trajectories of R- and S- $(MBA^+)_2SnI_4$ coordinates.
The calculated spectra of the tin chiral perovskite at the HSE06/LANL2DZ show a good agreement in terms of the band shapes and the signs of excitonic couplings, despite a systematic blue-shift of the vertical energies that can be attributed to the high extent of the density of states localized within the tin cation and the chiral ligand (Figure 1a).
It is worth noting that the ECD spectra of the tin-based chiral perovskites are characterized by the presence of a series of excitonic lines that are well reproduced by the TD-DFT simulations. These chiroptical signals can be rationalized by considering that the chirality transfer (and organic-inorganic coupling) is stronger in tin-based chiral LDHPs than the lead-based ones, as already discussed in PDOSs analysis (Figure 1). Noteworthy the calculated absorption electronic transitions of lead- and tin-based perovskite models, well fit the bands positions predicted through the DOSs calculations on the same clusters, as shown in Figure S1 of Supplementary Information.

Computational Details

Periodic simulations and density of state calculations

The density of states of the $(MBA^+)_2PbI_4$ and $(MBA^+)_2SnI_4$ chiral perovskites were computed at the PBE[48] level of theory by including the spin-orbit coupling as implemented in Quantum Espresso package.[55,56] The Pb.rel-pbe-dn-rrkjus_psl.1.0.0.UPF, I.pbe-n-rrkjus_psl.1.0.0.UPF,

C.pbe-rrkjus.UPF, H.pbe-rrkjus.UPF, N.pbe-rrkjus.UPF, Sn.rel-pbe-dn-rrkjus_psl.1.0.0.UPF ultrasoft pseudopotentials from http://www.quantum-espresso.org[55,56] were used during the calculations. The crystallographic coordinates of the $(MBA^+)_2PbI_4$ and $(MBA^+)_2SnI_4$ chiral perovskites were optimized starting from the crystallographic cell parameters reported by Jana et al.[41] and by Lu et al.[44] respectively and available in the Cambridge Crystallographic Data Center (CCDC) database with the deposition number of 2015617 for the lead-based chiral perovskite and of 1994338 for the tin analogue. Electronic densities of states were calculated after optimizing the atomic positions under periodic boundary conditions at fixed experimental cell parameters and with a vacuum of 14 Å orthogonal to the periodic layer. The density of states calculations were then performed on the optimized coordinates in periodic boundary conditions by maintaining the same cell parameters, a kinetic energy cutoff of 400 Ry for the wave functions and a kinetic energy cutoff of 35 Ry for the charge density. The total densities of states were then projected on I, Pb, Sn, and C atoms. The density of states were calculated at the same level of theory for the tin-based and lead-based chiral perovskites by excluding the atoms belonging to the inorganic layers and keeping the coordinates of the organic layer in the original positions. Such total densities of states were then projected on the C atoms of the chiral organic ligand. For the calculations of the electron density differences, the electron densities were computed at PBE level on i) the whole lead- and tin-based perovskites, on ii) the organic ligands and on iii) the octahedral layers, separately within Quantum espresso package 7.0.[55,56]

Ab-initio molecular dynamics of cluster models

The starting coordinates representing molecular clusters were constructed starting from the crystallographic coordinates of the $(MBA^+)_2PbI_4$ and $(MBA^+)_2SnI_4$ chiral perovskites experimentally available[41,44] and by considering two inorganic $[MI_6]^{4-}$ (with $M=Pb^{2+}$ or Sn^{2+}) octahedral layers and four chiral MBA^+ chains of the R and S enantiomeric models in order to maintain the 2:1 stoichiometric ligand-perovskite ratio experimentally reported. The iodine atoms of the crystallographic cell allow saturating the lead and tin coordination spheres.
In order to evaluate if the constructed models well represent the periodic systems, density of state calculations were performed on such molecular clusters and compared with the density of states computed in periodic boundary conditions (Figure S1 of Supporting Information).
All the constructed enantiomeric LDHP models were firstly optimized at PBE[48] level of theory and by using the Pb.pbe-dn-rrkjus_psl.1.0.0.UPF, I.pbe-n-rrkjus_psl.1.0.0.UPF, C.pbe-rrkjus.UPF, H.pbe-rrkjus.UPF, N.pbe-rrkjus.UPF, Sn.pbe-dn-rrkjus_psl.1.0.0.UPF, ultrasoft pseudpotentials from http://www.quantum-espresso.org.[55,56] The optimized coordinates of the constructed models are reported in a separated ZIP file of the Supporting Information.
The density of state calculations were then performed on the optimized cluster models by including a vacuum of 14 Å in the xyz directions, a kinetic energy cutoff of 400 Ry for the wave functions and a kinetic energy cutoff of 35 Ry for the charge density. The same calculations were performed also by including spin-orbit coupling, by using Pb.rel-pbe-dn-rrkjus_psl.1.0.0.UPF, I.pbe-n-rrkjus_psl.1.0.0.UPF, C.pbe-rrkjus.UPF, H.pbe-rrkjus.UPF, N.pbe-rrkjus.UPF, Sn.rel-pbe-dn-rrkjus_psl.1.0.0.UPF, ultrasoft pseudpotentials from http://www.quantum-espresso.org[55,56], but no significant differences were predicted, as shown in Figure S1. A convergence test on the vacuum dimension were performed by considering vacuum values of 12 Å, 14 Å and 16 Å in the xyz directions (Figure S2 of Supporting Information).
The energy and temperature evolution plots of the computed ab-initio trajectories are reported in Figure S3 and S4 of Supporting Information.

Circular dichroism calculations of cluster models

The UV-vis and ECD spectra were calculated from a collection of configurations extracted from the ab-initio molecular dynamics trajectories, following the simulation workflows we developed to predict chiroptical properties[57] and described below.
A set of exchange density functionals was preliminary tested with Gaussian16 software,[58] also including those counting for Van der Waals D3 dispersion and reported in Table S1 of the Supporting Information. These tests indicates that PBE-based functionals particularly the HSE06[59] density functional, are those that well describe the CD spectra of the LDHPs under study, in agreement with the general accepted simulation *ab-initio* protocol derived on achiral perovskites and previously reported.[60] Simulations accounting for spin-orbit coupling were tested using Douglas-Kroll-Hess[61] 4th order relativistic calculation including spin-orbit terms. However the latter largely increase the computational cost with no sizeable differences observed at HSE06[59] level.
Considering such evidences, excitation energies, oscillator and rotatory strengths were computed for the coordinates selected from the ab-initio trajectories at HSE06[59]/LANL2DZ level of theory, by considering the first 100 electronic states for the lead-based coordinates and the first 200 electronic states for the tin-based ones, with Gaussian16 software.[58] The calculations of the UV-vis and ECD spectra at a given excitation wavelength have been carried out assuming Gaussian bands with 900 cm^{-1} full width at half-height for all transitions.
The rotational strengths were computed at HSE06/LANL2DZ with Gaussian16 software[58] for the S-enantiomers of the lead- and tin-based cluster models, by considering the PBE-optimized coordinates within Quantum Espresso package.[55,56] The same computations were then repeated by neglecting the inorganic layers and by maintaining the organic ligands in the original optimized positions.
In order to verify if the SOC effects have significant contributions in the ECD spectra simulations calculated on the cluster coordinates of the lead- and tin-based LDHPs, ab-initio molecular dynamics were performed at PBE[48] level of theory by including SOC contributions for the S-enantiomers of LDHPs, by using Pb.rel-pbe-dn-rrkjus_psl.1.0.0.UPF, I.pbe-n-rrkjus_psl.1.0.0.UPF, C.pbe-rrkjus.UPF, H.pbe-rrkjus.UPF, N.pbe-rrkjus.UPF, Sn.rel-pbe-dn-rrkjus_psl.1.0.0.UPF, ultrasoft pseudpotentials from http://www.quantum-espresso.org[55,56] in the NVT ensemble for a total time of simulation of 2 ps with a stepsize of 1 fs. A temperature of 300 K was enforced during the simulation by using the Nosé-

Hoover thermostat as implemented in Quantum Espresso.[55,56] A vacuum of 14 Å in the xyz directions, a kinetic energy cutoff of 400 Ry for the wave functions and of 35 Ry for the charge density were set during the ab-initio molecular dynamics simulations.
The ECD spectra were calculated from a collection of configurations extracted from the ab-initio molecular dynamics trajectories, thereby computing excitation energies and rotatory strengths at HSE06[59]/LANL2DZ level of theory. The first 100 electronic states were considered for the lead-based coordinates and the first 200 electronic states for the tin-based ones, with Gaussian16 software.[58] Scalar relativistic effects were included by using the Douglas-Kroll-Hess method[49] and the simulated ECD spectra are reported in Figure S5 of the Supporting Information.

Conclusions

Overall, ab-initio molecular dynamics, projected density of state calculations, TD-DFT simulations and ECD spectra predictions consistently give indications on how the chiral bias affects the inorganic octahedra and how it differs in lead and tin chiral perovskites. The comparative analyses of the density of states of the hybrid perovskite and the ligands alone, unambiguously show a metal-ligand interaction, with overlaps of their electronic levels and the shift of levels above the Fermi level related to aromatic carbons of the ligands.
The difference in tin and lead stems from the extent of the electronic coupling. In fact, the chiral transfer appears larger for tin than for lead, both considering the PDOS of the isolated ligands and the hybrid system, together with the rotational strengths calculated for the isolated ligands and for the hybrid systems. Furthermore, the large electronic coupling between the chiral ligands and the tin octahedra is caused from a radically different assembling of the chiral ligands encapsulated in the tin perovskite, resulting in a highly distorted coordination allowing for CH-π interactions.
These observations have been obtained by ab initio calculations based on molecular dynamics, electronic structure DFT and TD-DFT. All of them elucidated the chiroptical features of 2D lead- and tin-based chiral perovskites, the R- and S-$(MBA^+)_2PbI_4$ and R- and S-$(MBA^+)_2SnI_4$. By analyzing the DOSs of the hybrid systems compared to the isolated components we concluded that the main factor controlling the resulting chiroptical features is a chirality transfer event originated from a metal-ligand interaction. This hybrid coupling is more effective for the tin-based chiral LDHPs showing an ECD pattern featured by excitonic couplings in the range of 300-500 nm. The lesser metal-ligand coupling in the lead chiral perovskite can explain the red-shift of the CD spectra within the range of 500-600 nm.

Author Contributions

MF carried out the simulations, AP and AM planned the chiral perovskite simulation workflows, MF, AM and AP wrote the manuscript.

Conflicts of interest

There are no conflicts to declare.

Acknowledgements

The Italian Ministry for University and Research (MUR) and University “Magna Græcia” of Catanzaro are acknowledged for the financial support under PON “RICERCA E INNOVAZIONE” 2014–2020, ASSE IV “ISTRUZIONE E RICERCA PER IL RECUPERO” AZIONE IV.4 “DOTTORATI E CONTRATTI DI RICERCA SU TEMATICHE DELL’INNOVAZIONE” D.M. 1062/2021 program and under the research program PRIN 2017WBZFHL_003. The ISCRA supercomputing initiative is also acknowledged for providing computational resources. AM acknowledges CNR for Project B55F21000620005, MUR for Project PON04a2_00490 B22I12000280001 and ICSC – Centro Nazionale di Ricerca in High Performance Computing, Big Data and Quantum Computing, funded by European Union – NextGenerationEU - PNRR, Missione 4 Componente 2 Investimento 1.4".

Notes and references

1. A. Kojima, K. Teshima, Y. Shirai, T. Miyasaka, *J. Am. Chem. Soc.,* 2009, **131**, 6050-6051.
2. M. M. Lee, J. Teuscher, T. Miyasaka, T. N. Murakami, H. J. Snaith, *Science*, 2012, **338**, 643-647.
3. Z. Li, T. R. Klein, D. H. Kim, M. Yang, J. J. Berry, M. F. A. M. van Hest, K. Zhu, *Nat. Rev. Mat.*, 2018, **3**, 18017.
4. Y. Fu, H. Zhu, J. Chen, M. P. Hautzinger, X. Y. Zhu, S. Jin, *Nat. Rev. Mat.*, 2019, **4**, 169-188.
5. N. Wang, L. Cheng, R. Ge, S. Zhang, Y. Miao, W. Zou, C. Yi, Y. Sun, Y. Cao, R. Yang, Y. Wei, Q. Guo, Y. Ke, M. Yu, Y. Jin, Q. Ding, D. Di, L. Yang, G. Xing, H. Tian, C. Jin, F. Gao, *Nat. Photonics*, 2016, **10**, 699-704.
6. X. Yang, X. Zhang, J. Deng, Z. Chu, Q. Jiang, J. Meng, P. Wang, L. Zhang, Z. Yin, J. You, *Nat. Commun.*, 2018, **9**, 570.
7. Y. Zou, Q. Huang, Y. Yang, M. Ban, S. Li, Y. Han, T. Wu, Y. Tan, X. Gao, T. Song, B. Sun, *Adv. Mater. Interfaces* 2018, **5**, 1801030.
8. J. Byun, H. Cho, C. Wolf, M. Jang, A. Sadhanala, R. H. Friend, H. Yang, T. W. Lee, *Adv. Mater.,* 2016, **28**, 7515-7520.

9. J. Xing, Y. Zhao, M. Askerka, L. N. Quan, X. Gong, W. Zhao, J. Zhao, H. Tan, G. Long, L. Gao, Z. Yang, O. Voznyy, J. Tang, Z. –H. Lu, Q. Xiong, E. –H. Sargent, *Nat. Commun*., 2018, **9**, 3541.
10. W. Su, Y. Fanglong, *Trends in Chemistry*, 2022, **4**, 965-968.
11. B. R. Sutherland, E. -H. Sargent, *Nat. Photonics*, 2016, **10**, 295-302.
12. H. Zhu, Y. Fu, F. Meng, X. Wu, Z. Gong, Q. Ding, M. V. Gustafsson, M. T. Trinh, S. Jin, X. Y. Zhu, *Nat. Mater.,* 2015, **14**, 636-642.
13. C. M. Raghavan, T. P. Chen, S. S. Li, W. L. Chen, C. Y. Lo, Y. M. Liao, G. Haider, C. C. Lin, C. C. Chen, R. Sankar, Y. M. Chang, F. C. Chou, C. W. Chen, *Nano Lett.,* 2018, **18**, 3221-3228.
14. J. Li, J. Wang, Y. Zhang, H. Wang, G. Lin, X. Xiong, W. Zhou, H. Luo, D. Li, *2D Mater.,* 2018, **5**, 021001.
15. Y.Chen, Y. Sun, J. Peng, J. Tang, K. Zheng, Z. Liang, *Adv. Mater.*, 2018, **30**, 1703487.
16. L. Ji, H.-Y. Hsu, J. C. Lee, A. J. Bard, E. T. Yu, *Nano Lett.,* 2018, **18**, 994-1000.
17. L. Dou, Y. M. Yang, J. You, Z. Hong, W.-H. Chang, G.Li, Y.Yang, *Nat. Commun.,* 2014, **5**, 5404.
18. K. Leng, I. Abdelwahab, I. Verzhbitskiy, M. Telychko, L. Chu, W. Fu, X. Chi, N. Guo, Z. Chen, Z. Chen, C. Zhang, Q.-H. Xu, J. Lu, M. Chhowalla, G. Eda, K. P. Loh, *Nat. Mater.,* 2018, **17**, 908-914.
19. J. Li, J. Wang, J. Ma, H. Shen, L. Li, X. Duan, D. Li, *Nat. Commun.*, 2019, **10**, 806.
20. D. H. Cao, C. C. Stoumpos, O. K. Farha, J. T. Hupp, M. G. Kanatzidis, *J. Am. Chem. Soc.,* 2015, **137**, 7843-7850.
21. N. J. Jeon, H. Na, E. H. Jung, T. –Y. Yang, Y. G. Lee, G. Kim, H.-W. Shin, S. I. Seok, J. Lee, J. Seo, *Nat. Energy*, 2018, **3**, 682-689.
22. A. Filippetti, S. Kahmann, C. Caddeo, A. Mattoni, M. Saba, A. Bosin, M. A. Loi, *J. Mater. Chem. A*, 2021,**9**, 11812-11826.
23. G. Niu, X. Guo, L. Wang, *J. Mater. Chem. A* 2015, **3**, 8970-8980.
24. I. C. Smith, E. T. Hoke, D. Solis-Ibarra, M. D. McGehee, H. I. Karunadasa, *Angew. Chem*. 2014, **126**, 11414-11417.
25. C. C. Stoumpos, D. H. Cao, D. J. Clark, J. Young, J. M. Rondinelli, J. I Jang, J. T. Hupp, M. G. Kanatzidis, *Chem. Mater.* 2016, **28**, 2852-2867.
26. J. Wang, J. Li, Q. Tan, L. Li, J. Zhang, J. Zang, P. Tan, J. Zhang, D. Li, *J. Phys. Chem. Lett.* 2017, **8**, 6211-6219.
27. S. Wen, Y. Fanglong, "Two-dimensional superlattices intercalated with chiral molecules for spin selectivity." *Science China Materials* (2022): 1-2
28. Y. Shi, P. Duan, S. Huo, Y. Li, M. Liu, *Adv. Mater.* 2018, **30**, 1705011.
29. C. Yuan, X. Li, S. Semin, Y. Feng, T. Rasing, J. Xu, *Nano Lett.* 2018, **18**, 5411.
30. G. Long, C. Jiang, R. Sabatini, Z. Yang, M. Wei, L. N. Quan, Q. Liang, A. Rasmita, M. Askerka, G. Walters, X. Gong, J. Xing, X. Wen, R. Quintero-Bermudez, H. Yuan, G. Xing, X. R. Wang, D. Song, O. Voznyy, M. Zhang, S. Hoogland, W. Gao, Q. Xiong, E. H. Sergent, *Nat. Photonics*, 2018, **12**, 528-533.
31. Y. Yang, R. C. Da Costa, M. J. Fuchter, A. J. Campbell, *Nat. Photonics* 2013, **7**, 634-638.
32. M. W. Heindl, T. Kodalle, N. Fehn, L. K. Reb, S. Liu, C. Harder, M. Abdelsamie, L. Eyre, I. D. Sharp, S. V. Roth, P. Muller-Buschbaum, A. Kartouzian, C. M. Sutter-Fella, F. Deschler, *Adv. Opt. Mat.* 2022, **10 (14)**, 2200204.
33. Y. Zheng, X. Han, P. Cheng, X. Jia, J. Xu, X.-H. Bu, *J. Am. Chem. Soc.* 2022, **144 (36),** 16471-16479
34. J. M. Urban, A. Jouaiti, N. Gruber, G. Delport, G. Trippè-Allard, J.-F. Guillemoles, E. Deleporte, S. Ferlay, D. Garrot, *J. Mat. Chem. C*, 2022, **10(34),** 12436-12443.
35. D. G. Billing, A. Lemmerer, *CrystEngComm,* 2006, **8**, 686-695.
36. J. Ahn, E. Lee, J. Tan, W. Yang, B. Kim, J. Moon, *Mat. Horiz.* 2017, **4**, 851-856.
37. G. Long, R. Sabatini, M. I. Saidaminov, G. Lakhwani, A. Rasmita, X. Liu, E. H. Sargent, W. Gao, *Nat. Rev. Mat.* 2020, 5, 423-439.
38. A. Forde, D. Ghosh, D. Kilin, A. C. Evans, S. Tretiak, A. J. Neukirch, *J. Phys. Chem. Lett.* 2022, **13**, 686-693.
39. A. Pietropaolo, A. Mattoni, G. Pica, M. Fortino, G. Schifino, G. Grancini, *Chem*, 2022,**8**, 1231-1253.
40. R. Chakraborty, P. K. Rajput, G. M. Anilkumar, S. Maqbool, R. Das, A. Rahman, P. Mandal, A. Nag, *J Am Chem Soc.* 2023, **145(2)**, 1378-1388.
41. M. K. Jana, R. Song, H. Liu, D. R. Khanal, S. M. Janke, R. Zhao, C. Liu, Z. V. Vardeny, V. Blum, D. B. Mitzi, *Nat. Commun.,* 2020, **11**, 4699.
42. S. Ma, S., Y.-K. Jung, J. Ahn, J. J. Kyhm, J. Tan, H. Lee, G. Jang, C. U. Lee, A. Walsh, J. Moon*, Nat Commun,* 2022*,* **13**, 3259.
43. J. Ma, C. Fang, C. Chen, L. Jin, J. Wang, S. Wang, J. Tang, D. Li, *ACS Nano*, 2019, **13**, 3659-3665.
44. H. Lu, C. Xiao, R. Song, T. Li, A. E. Maughan, A. Levin, R. Brunecky, J. J. Berry, D.B. Mitzi, V. Blum, M. C. Beard, *J. Am. Chem. Soc.* 2020, **142,** 13030-13040.
45. H. Duim, M. A. Loi, *Matter*, 2021, **4**, 3835-3851.
46. H. Lu, Z. V. Vardeny, M. C. Beard, *Nat. Rev. Chem*., 2022, **6**, 470-485.
47. G. Long, G. Adamo, G., J. Tian, M. Klein, H. N. S. Krishnamoorty, E. Feltri, H. Wang, C. Soci, Nat. Commun., 2022, **13**, 1551.
48. M. Ernzerhof, J. P. Perdew, *J. Chem. Phys.,*1998, **109**, 3313.
49. Dal Corso A., Mosca Conte A. *Phys. Rev. B*, 2005, **71**, 115106.
50. F. Lédée, P. Audebert, G. Trippé-Allard, L. Galmiche, D. Garrot, J. Marrot, J.S. Lauret, E. Deleporte, C. Katan ,J. Even, C. Quarti. *Mater. Horiz.*, 2021,**8**, 1547-1560.
51. M.I. Dar, G. Jacopin, S. Meloni, A. Mattoni, N. Arora, A. Boziki, S. M. Zakeeruddin, U. Rothlisberger, M. Grätzel. *Sci Adv.* 2016 2, e1601156.
52. E. Mosconi, F. De Angelis *ACS Energy Lett.* 2016, **1**, 182–188
53. C. Motta, F. El-Mellouhi, S. Sanvito. *Sci Rep.* 2015 **5**, 12746.
54. A. Pietropaolo, Y. Wang, T. Nakano. Angew Chem Int Ed Engl. 2015, **54**, 2688-2692.
55. P. Giannozzi, S. Baroni, N. Bonini, M. Calandra, R. Car, C. Cavazzoni, D. Ceresoli, G. L. Chiarotti, M. Cococcioni, I. Dabo, A. Dal Corso, S. de Gironcoli, S. Fabris, G. Fratesi, R. Gebauer, U. Gerstmann, C. Gougoussis, A. Kokalj, M. Lazzeri, L. Martin-Samos, N. Marzari, F. Mauri, R. Mazzarello, S. Paolini, A. Pasquarello, L. Paulatto, C. Sbraccia, S. Scandolo, G. Sclauzero, A. P. Seitsonen, A. Smogunov, P. Umari, R. M. Wentzcovitch*, J.Phys. Condens. Matter,* 2009*,* **21**, 395502.
56. P. Giannozzi, O. Andreussi, T. Brumme, O. Bunau, M. Buongiorno Nardelli, M. Calandra, R. Car, C. Cavazzoni, D. Ceresoli, M. Cococcioni, N. Colonna, I. Carnimeo, A. Dal Corso, S. de Gironcoli, P. Delugas, R. A. DiStasio Jr, A. Ferretti, A. Floris, G. Fratesi, G. Fugallo, R. Gebauer, U. Gerstmann, F. Giustino, T. Gorni, J Jia, M. Kawamura, H.-Y. Ko, A. Kokalj, E. Küçükbenli, M .Lazzeri, M. Marsili, N. Marzari,

F. Mauri, N. L. Nguyen, H.-V. Nguyen, A. Otero-de-la-Roza, L. Paulatto, S. Poncé, D. Rocca, R. Sabatini, B. Santra, M. Schlipf, A. P. Seitsonen, A. Smogunov, I. Timrov, T. Thonhauser, P. Umari, N. Vast, X. Wu, S. Baroni, *J.Phys. Condens. Matter,* 2017*,* **29**, 465901.
57. P. Wu, A. Pietropaolo, M. Fortino, S. Shimoda, K. Maeda, T. Nishimura, M. Bando, N. Naga, T. Nakano, *Angew. Chem. Int. Ed.* 2022, **61**, e202210556.
58. Gaussian 16, Revision C.01, M. J. Frisch, G. W. Trucks, H. B. Schlegel, G. E. Scuseria, M. A. Robb, J. R. Cheeseman, G. Scalmani, V. Barone, G. A. Petersson, H. Nakatsuji, X. Li, M. Caricato, A. V. Marenich, J. Bloino, B. G. Janesko, R. Gomperts, B. Mennucci, H. P. Hratchian, J. V. Ortiz, A. F. Izmaylov, J. L. Sonnenberg, D. Williams-Young, F. Ding, F. Lipparini, F. Egidi, J. Goings, B. Peng, A. Petrone, T. Henderson, D. Ranasinghe, V. G. Zakrzewski, J. Gao, N. Rega, G. Zheng, W. Liang, M. Hada, M. Ehara, K. Toyota, R. Fukuda, J. Hasegawa, M. Ishida, T. Nakajima, Y. Honda, O. Kitao, H. Nakai, T. Vreven, K. Throssell, J. A. Montgomery, Jr., J. E. Peralta, F. Ogliaro, M. J. Bearpark, J. J. Heyd, E. N. Brothers, K. N. Kudin, V. N. Staroverov, T. A. Keith, R. Kobayashi, J. Normand, K. Raghavachari, A. P. Rendell, J. C. Burant, S. S. Iyengar, J. Tomasi, M. Cossi, J. M. Millam, M. Klene, C. Adamo, R. Cammi, J. W. Ochterski, R. L. Martin, K. Morokuma, O. Farkas, J. B. Foresman, and D. J. Fox, Gaussian, Inc., Wallingford CT, 2016.
59. J. Heyd, G. Scuseria, J. Chem. Phys*.*, 2004, **121**, 1187.
60. H. Q. Pham, R. J. Holmes, E. S. Aydil, L. Gagliardi, *Nanoscale*, 2019, **11**, 11173.
61. F. E. Jorge, A. Canal Neto, G. G. Camiletti, S. F. Machado, *J. Chem. Phys.,* 2009, **130**, 064108.